



Universidad Autónoma
de Madrid

Biblos-e Archivo
Repositorio Institucional UAM

Repositorio Institucional de la Universidad Autónoma de Madrid

<https://repositorio.uam.es>

Esta es la **versión de autor** del artículo publicado en:
This is an **author produced version** of a paper published in:

Journal of Materials Chemistry C 9.13 (2021): 4682-4694

DOI: <https://doi.org/10.1039/d1tc00329a>

Copyright: © 2021 The Royal Society of Chemistry

El acceso a la versión del editor puede requerir la suscripción del recurso

Access to the published version may require subscription

Self-powered broadband hybrid organic-inorganic photodetectors based on PEDOT:PSS and silicon micro-nanostructures

Rehab Ramadan^{1,2,3,*}, Vicente Torres-Costa^{1,3} and Raúl J. Martín-Palma^{1,3}

¹ Departamento de Física Aplicada, Universidad Autónoma de Madrid, 28049 Madrid, Spain

² Department of Physics, Faculty of Science, Minia University, Minia 61519, Egypt

³ Instituto de Ciencia de Materiales Nicolás Cabrera, Universidad Autónoma de Madrid, 28049 Madrid, Spain

* Correspondence: rehab.ramadan@uam.es; Tel.: +34-914974919

Abstract

Hybrid organic-inorganic self-powered photodetectors with three different configurations were fabricated and their optoelectronic performance was determined. Si being the inorganic active layer and the transparent conductor poly(3,4- ethylenedioxythiophene) polystyrene sulfonate (PEDOT:PSS) the organic layer. The basic photodetector structure under study is Au/PEDOT:PSS/Si/Al. This device shows high responsivity at low irradiation levels, as well as a wideband response in the visible and near-infrared wavelength ranges. To improve the performance of the device, the basic photodetector structure was modified by the addition of a nanostructured porous silicon (PSi) layer on top of the Si substrate. The modified Au/PEDOT:PSS/PSi/Si/Al devices have been found to show improved photoresponse under high irradiation levels together with narrowband spectral responsivity in the infrared region. To further improve the optoelectronic performance of the photodetectors, Si+PSi micro-arrays were used instead of single PSi layers, leading to devices with the structure Au/PEDOT:PSS/(Si+PSi micro-arrays)/Si/Al. These devices possess a much improved performance, showing a responsivity of 1172.87 mA/W, a specific detectivity of 5.81×10^{13} Jones, and a fast response speed of 396/412 μ s at 0 V bias under white-light illumination (100 μ W). Furthermore, a broadband spectral responsivity was achieved, with a maximum value of 473 mA/W at 853 nm. This improved photonic behavior is associated to the combined effect of an effective reduction of the reflectance due to the presence of PSi and an improvement of the electrical conduction given by the presence of heavily-doped Si regions.

Keywords: Self-powered photodetectors; Broadband photodetectors; Porous silicon; Micro-nanostructures; PEDOT:PSS; Hybrid organic-inorganic device; Spectral responsivity.

1. Introduction

Self-powered photodetectors possess high potential for use in numerous applications in such diverse fields as optical communications, biomedicine, gas sensing, and video imaging ^[1]. Depending on their wavelength response, there are selective and broadband photodetectors. Broadband photodetectors with high detection efficiency, fast speed, high operation stability, small size, and low cost possess an enormous commercialization potential.

In addition to the many semiconducting materials used for photodetection, hybrid organic-inorganic structures are being increasingly used due to their attractive optical and electrical properties ^[2-6]. Organic polymers like Poly(3-hexylthiophene) (P₃HT), [6,6]-phenyl-C₆₁-butyric acid methyl ester (PC₆₁BM) ^[7], poly(2,7-carbazole-alt-4,7-dithienyl-2,1,3-benzothiadiazole) ^[8], and poly(3,4-ethylenedioxythiophene) polystyrene sulfonate (PEDOT:PSS) ^[9,10] are extensively used, not only in photodetectors, but also in solar cells with a remarkable performance. In particular, PEDOT:PSS is one of the most successful conducting polymers. Thorough studies have been carried out on photodetectors based on hybrid PEDOT:PSS/n-type inorganic semiconductor structures which show a promising photoresponse. For instance, blue-sensitive photodetectors with the configuration PEDOT:PSS/SnO₂ microwires show a responsivity of 18.2 mA/W at 450 nm ^[10], while that of self-powered (PEDOT:PSS/Ga₂O₃) devices is 37.4 mA/W at 254 nm ^[11], and that of PEDOT:PSS/Si nanowire arrays based-self-powered photodetectors is 37.8 mA/W at 920 nm ^[12].

Aiming at their integration in current CMOS technology, it would be highly desirable to develop highly efficient silicon-based photodetectors in the visible. However, Si has an indirect bandgap and high optical losses ^[13]. Structural modifications have been introduced to the surface of Si by many researchers aiming at improving its optical

performance, including periodic nanostructures of Si (nanowires, quantum dots and pyramidal shapes) and randomly-textured structures such as porous silicon (PSi) [14-17]. However, texturing the surface of Si leads to some key disadvantages, i.e., (1) increased surface-to-volume ratio leading to increased electron-hole recombination rates, (2) fast surface oxidation rates, and (3) reduction of the electrical conductivity due to quantum confinement effects [18, 19].

The main aim of this work is to combine the good electrical properties of Si and the optical enhancement provided by PSi in one device. In this line, integrated micro-nanostructures consisting of ordered micro-arrays of PSi on the surface of Si, i.e., Si+PSi micro-arrays, were fabricated for their subsequent use as self-powered photodetectors. Three configurations of hybrid organic-inorganic PEDOT:PSS-Si self-powered photodetectors were fabricated and studied: the basic Au/PEDOT:PSS/Si/Al structure, where Au and Al provide front and back contacts, and two variants aimed at improving the optical performance of the devices: Au/PEDOT:PSS/PSi/Si/Al and Au/PEDOT:PSS/(Si+PSi micro-arrays)/Si/Al. The PEDOT:PSS layer serves at the same time as a transparent conductor, anti-reflective coating and hole transport layer [20], while Si, PSi/Si, and (Si+PSi micro-arrays)/Si are the photodetector active layers, respectively. The morphology, optical properties, and electrical transport properties of the three different photodetector configurations were analyzed. Furthermore, we compared their photoresponse in a wide range of incident light powers. The stability and reproducibility to pulsed light were examined at 0 V. Finally, the spectral responsivity was analyzed in a broad wavelength range.

2. Experimental

Single-side polished phosphorous-doped (n-type) silicon wafers of orientation <100> were used for the fabrication of three different types of self-powered photodetectors. The properties of the Si wafers are (1-10 Ω .cm) resistivity, (300 \pm 15 nm) thickness and surface roughness in the order of 0.1 nm. The wafers were cleaned by ultrasonication in ethanol, acetone and distilled water for 10 minutes each.

2.1 Electrochemical etching of PSi layer

Before the electrochemical etching of the PSi layers, 100 nm-thick Al back contacts were deposited by electron beam evaporation. The base pressure was 1.25×10^{-5} mbar and the evaporation time was 2 minutes. The Al thin films were subsequently annealed by rapid thermal processing (RTP) in nitrogen atmosphere for 5 minutes to turn the initial rectifying junction into an ohmic one. Afterward, the wafers were cut into 1.5×1.5 cm² pieces. Each sample was mounted in a sample holder with an exposed circular area of 0.785 cm². The native oxide layer was removed by immersing the polished side of Si substrate into HF/H₂O solutions (1:20 ratio) for 30 s. Afterwards, the samples were immersed in the etching solution consisting of a 1:1 HF (48 wt%)/Methanol (99 wt%) mixture. The anodization current density and time were set at 10 mA/cm² and 10 s, respectively. The etching process was carried out at room temperature and under illumination with a halogen lamp (60 W). Schematic representation of the electrochemical etching process was portrayed in a previous study ^[21].

2.2 Fabrication of (Si+PSi micro-arrays) structures

Fabrication of (Si+PSi micro-arrays) micro-nanostructures was executed in two steps. First, micropatterning of the photoresist was carried out on Si substrates using a UV-lithography process. Particularly, a negative photoresist thin film was deposited on a pre-cleaned Si substrate by spin coating at 3000 rpm for 30 s, followed by drying on a hot plate for 15 minutes at 70°C. A photomask with the required structure (rectangular patterns of 55×70 μm²) was fixed on the photoresist/Si stack and exposed to UV radiation for 3 minutes. Afterwards, the photoresist was developed in a NaOH (0.15 M) solution for 6 minutes and washed with distilled water. The developed micropattern of the photoresist/Si was then post-baked for 15 minutes at 70°C to improve the adhesion of the micropattern to the Si surface. The second step consists on the electrochemical etch of the exposed Si areas. Using the same etching conditions as described in sec. 2.1, PSi was fabricated in the exposed areas of Si, resulting in photoresist+PSi micro-arrays which were thoroughly washed with distilled water. The photoresist was lifted-off by immersing the sample in acetone for 10 minutes, and finally the samples were rinsed several times in ethanol and isopropanol to remove any residuals or contamination. Integrated micro-nanostructures of (Si+PSi micro-arrays) were obtained as a result of the

two processes (photolithography and electrochemical etching). A schematic view of the fabrication processes of the Si+PSi micro-array structures is shown in Figure 1.

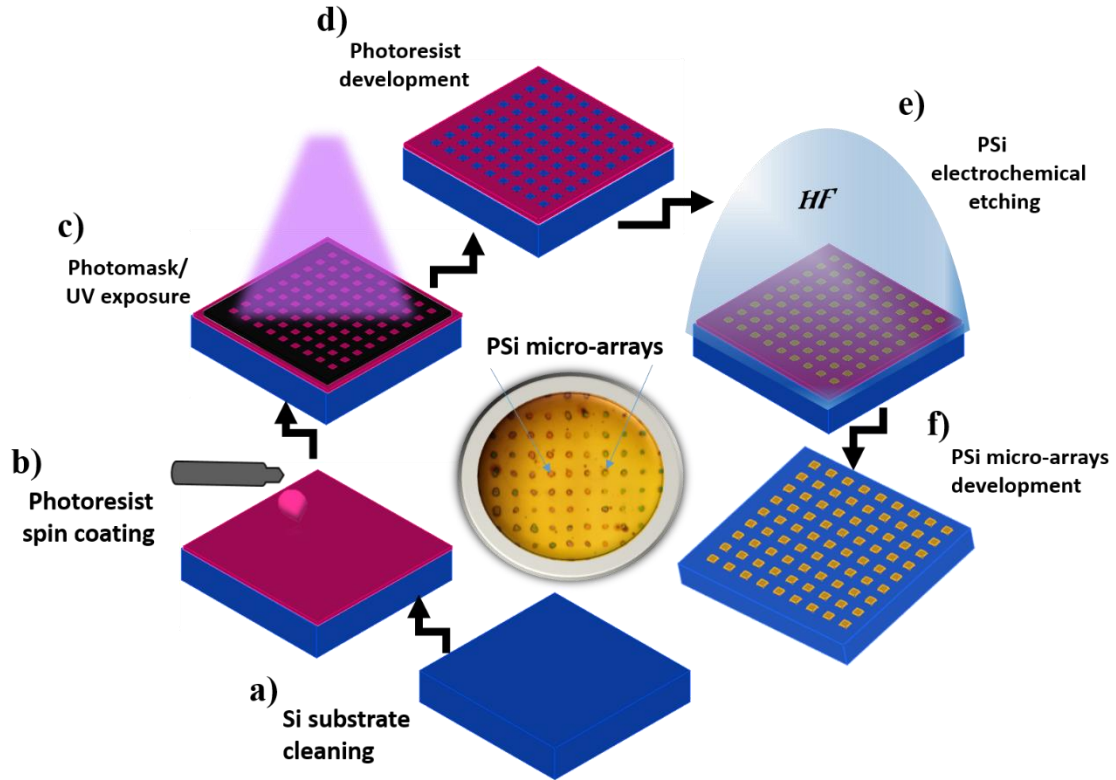


Figure 1: Schematic view of the photolithography process of Si substrate and the electrochemical etching of PSi micro-arrays on Si surface.

2.3 Spin coating of PEDOT:PSS thin films

Poly(3,4-ethylenedioxythiophene):polystyrene sulfonate (PEDOT:PSS 1.3wt%) polymer was purchased from Sigma Aldrich. Isopropyl alcohol (IPA) was used to increase the solubility of PEDOT:PSS solution. Dimethylsulfoxide (DMSO) (99.5%) assisted in improving the electrical conduction of the PEDOT:PSS films. Sulphuric acid (98%) was used to improve surface wettability of the active layers. Distilled water, ethanol (99%) and methanol (995) were used for cleaning purposes.

Highly transparent conducting layers of PEDOT:PSS were grown on three types of substrates, i.e., Si, PSi, and Si+PSi micro-arrays. The solution consisted of a 10:1:1 PEDOT:PSS/IPA/DMSO mixture. Before the deposition of the PEDOT:PSS thin films, 200 μ L of sulphuric acid were dropped on the surface of the substrate for 10 minutes to

increase surface wettability. Afterwards, samples were cleaned by ultrasonication in a distilled water bath for 10 minutes to remove any sulphuric acid residuals. 50 μ L of the PEDOT:PSS/IPA/DMSO solution was deposited on the pre-cleaned substrates by spin coating. For the deposition, the spin speed was 1000 rpm and the spin time was 60 s. Then, samples were heated at 100°C for 15 minutes to evaporate any solvents in the PEDOT:PSS layer. The process was repeated twice under the same conditions to obtain thicker PEDOT:PSS films.

2.4 Device configurations

Self-powered photodetectors with three different configurations were fabricated. These are Au/PEDOT:PSS/Si/Al, Au/PEDOT:PSS/PSi/Si/Al, and Au/PEDOT:PSS/(Si+PSi micro-arrays)/Si/Al. Au is the top contact, which is grown by DC-sputtering in an argon atmosphere using a patterned mask. The typical deposition pressure was 2×10^{-2} mbar and the typical plasma current was 20 mA, leading to a thickness of around 50 nm. The PEDOT:PSS thin films serve as transparent conductors. Si, PSi/Si, and (Si+PSi micro-arrays)/Si are the active layers in the self-powered photodetectors, while Al is the back contact (the evaporation conditions described in sec. 2.1). An illustration of the final structure of the three different photodetectors is presented in Figure 2, including FESEM images of the active layer for each device.

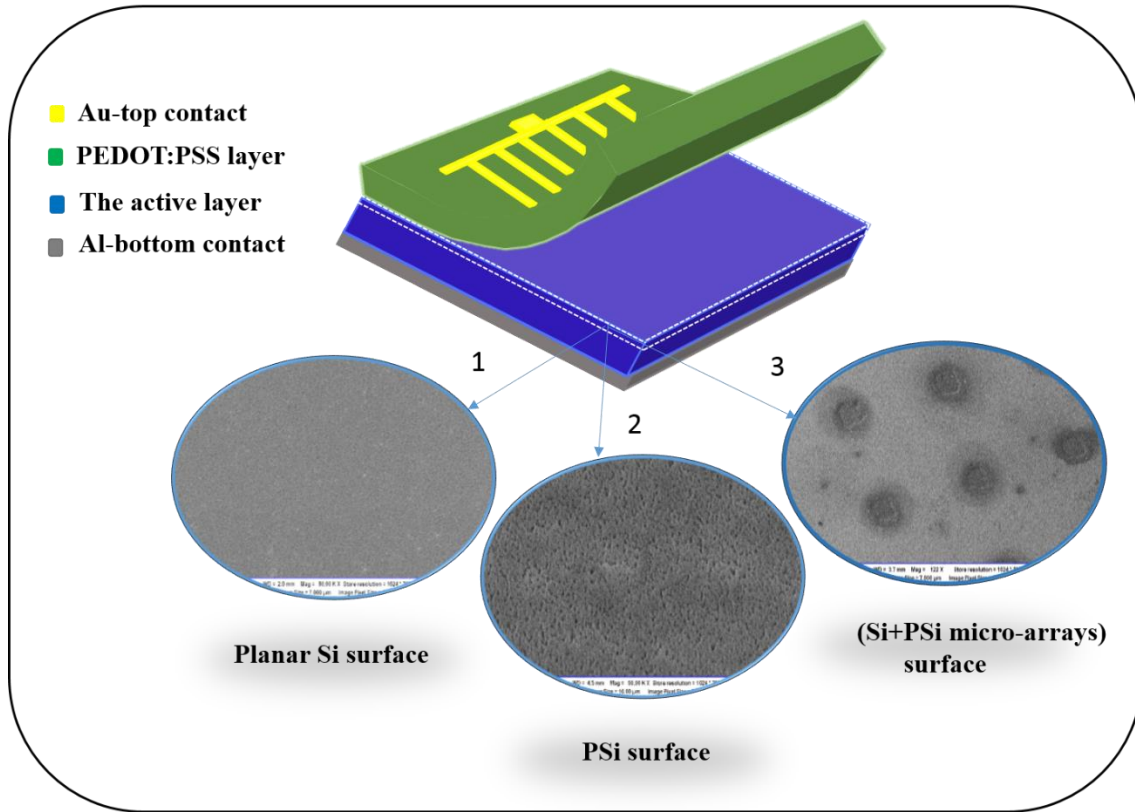


Figure 2: Schematic view of the fabricated self-powered photodetectors with the top and bottom contacts and FESEM top-view images of the active layer in the three devices.

2.5 Characterization techniques

The morphology of the PEDOT:PSS thin films and the active layers were studied by field emission scanning electron microscopy (FESEM) using a Philips XL-40FEG microscope operated at 5 kV.

Optical characterization in the UV–visible–near-infrared range (250–900 nm) was carried out using a Jasco V-560 double-beam spectrophotometer, equipped with an integrating sphere to avoid scattering losses.

The electrical and optoelectronic analysis of the photodetectors were carried out in a Bio-Logic SP-150 potentiostat. A homemade cell consisting of two movable copper probes

with a diameter of 0.5 mm and a copper base ($2 \times 2 \text{ cm}^2$) was used for all the electrical measurements. Current-voltage (I-V) curves in dark were carried out at a scan rate 10 mV/s and applied potential in the -0.5 to $+0.5 \text{ V}$ range. Electrochemical impedance spectroscopy (EIS) measurements were executed without external voltage and in the frequency 200 mHz to 1 MHz range.

A solar simulator (LCS-100 Solar Simulator-Model 94011A), with an adjustable illumination output power was used for photoresponse measurements. I-V curves under illumination were recorded in a wide range of incident light powers: 0.1, 1, 5, 15, 30, 50, 80, and 100 mW/cm^2 . Time-dependent current (I-t) curves (ON/OFF response) were recorded under the same incident light powers (0.1, 1, 5, 15, 30, 50, 80, and 100 mW/cm^2), every $2 \text{ }\mu\text{A}$ with time steps of $dt = 0.15 \text{ s}$ at 0 V bias. The response speed of the photodetectors was examined every 20 ms by a light source of intensity ($400 \text{ }\mu\text{W}$).

The spectral responsivity in the 300 to 1200 nm wavelength range was carried out at 0 V bias using a dual digital lock-in amplifier (Signal Recovery 7225) at a chopper frequency of 300 Hz. Illumination was provided by an Acton Research Corporation Tungsten-Deuterium dual light source (model TDS-429) and a SpectraPro 150 monochromator equipped with two interchangeable diffraction gratings (1200 lines/mm) was used to select the wavelength. The photoresponse of the devices to single-wavelength light was examined by determining the I-t curves (i.e., ON/OFF response) at 0 V bias and in different wavelength regions by adjusting the monochromatic light.

3. Results and discussion

Self-powered photodetectors with three different configurations were fabricated for the subsequent evaluation of their optoelectronic performance. The structure of these devices was described in the experimental section.

3.1 Morphological characterization

As a first step toward the analysis of the overall performance of the self-powered photodetectors, their morphology was analyzed by FESEM, as depicted in Figures 3 and

4. Figure 3.a shows a typical cross-sectional image of the PEDOT:PSS layer grown on the flat Si surface, which confirms a uniform coverage of the underlying Si substrate with a 90 nm thick film. Figure 3.b shows a characteristic cross-sectional view of the PEDOT:PSS/PSi/Si interface, from which it can be noted that 30 nm PSi layer shows a columnar structure with typical pore diameters in the 5 nm to 10 nm range. Furthermore, the PEDOT:PSS thin films grown on the PSi surface show a good homogeneity, with a thickness of around 80 nm. The inset of Figure 3.b shows that the pores of the PSi layer are partially filled with PEDOT:PSS, which explains the fact that the PEDOT:PSS layer is thinner than when grown on flat Si.

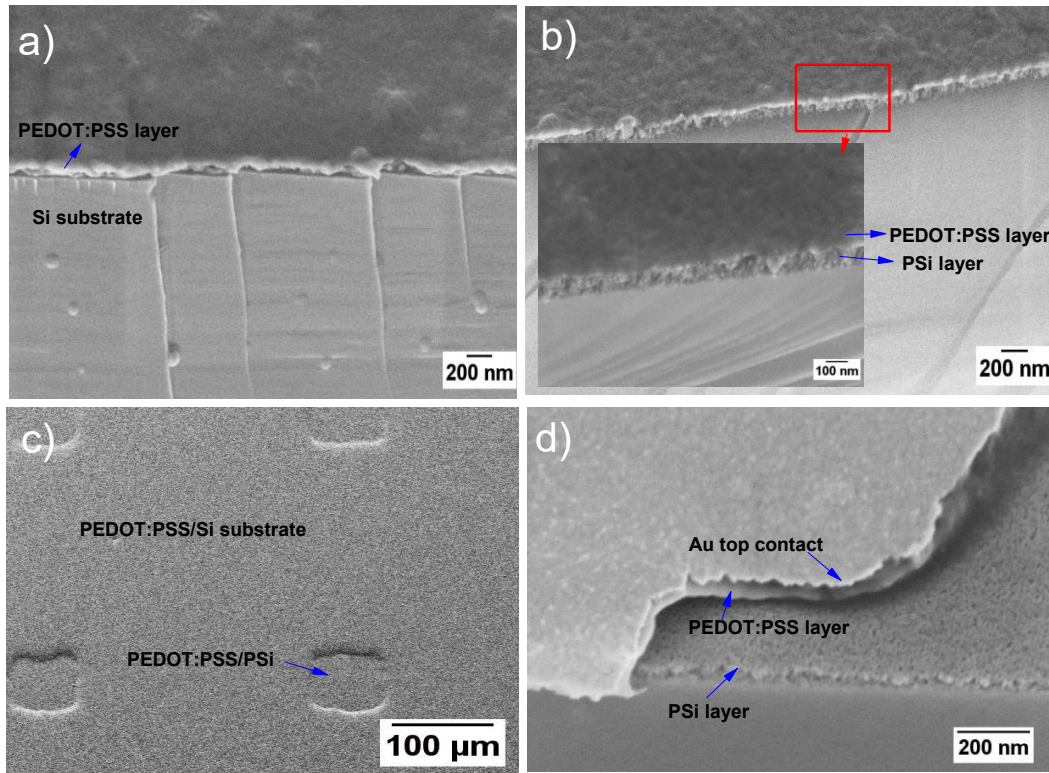


Figure 3: Typical FESEM images of PEDOT:PSS/active layers of the Si-based photodetectors. a) Cross-sectional view of PEDOT:PSS/Si interface, b) Cross-sectional view of PEDOT:PSS/PSi/Si interfaces, c) Top-view of PEDOT:PSS/(Si+PSi micro-arrays) surface, d) cross-sectional view of Au/PEDOT:PSS/PSi interfaces.

A top view of a PEDOT:PSS/(Si+PSi micro-arrays) surface is shown in Figure 3.c, showing a homogeneous surface coverage. Again, the partial infiltration of PEDOT:PSS into the PSi pores is revealed by the changes in surface height at the PSi locations. Figure

3.d shows a characteristic cross-sectional view of the Au top contact, PEDOT:PSS layer and PSi layer. The thickness of these layers are 50, 80, and 30 nm, respectively.

Figures 4 portrays typical FESEM images of the Si+PSi micro-arrays at different magnifications. Figure 4.a shows an overview of the PSi micro-arrays after photoresist development during lithography process. The distance between the two micropatterns is 225 μm and the surface area of the rectangular micro-arrays is $55 \times 70 \mu\text{m}^2$. Detailed views at different magnification of a single micro-array are depicted in Figures 4.b, 4.c and 4.d.

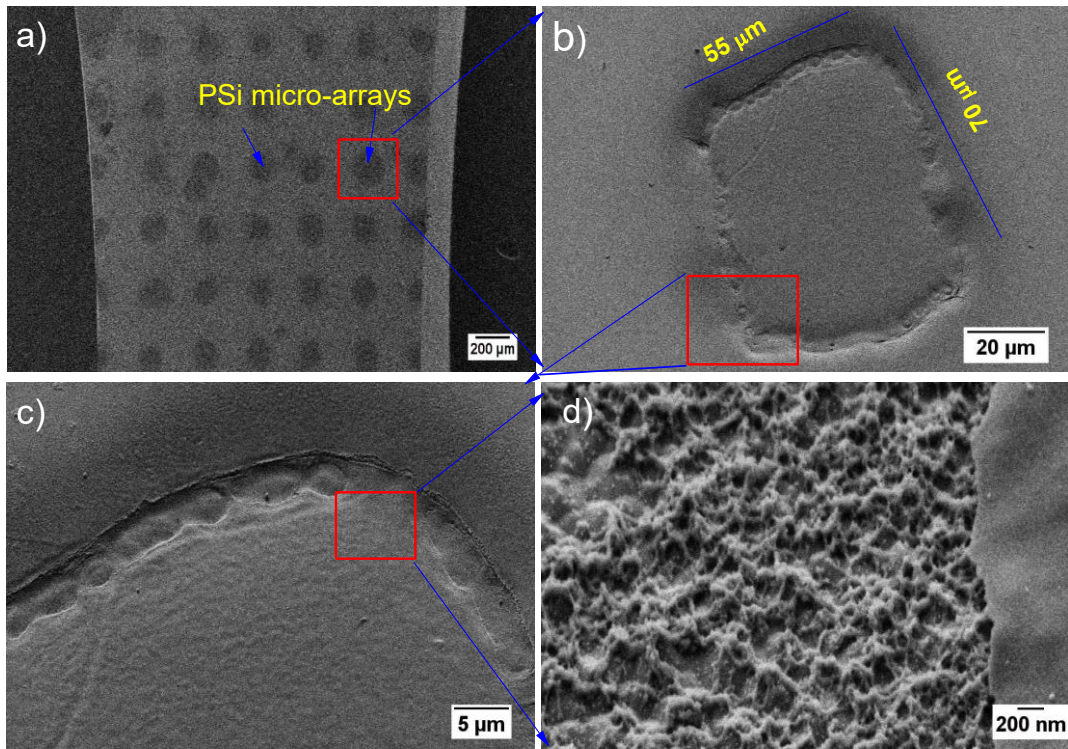


Figure 4: Typical top-views of the (Si+PSi micro-arrays) structure at different magnifications. a) An overview of PSi micro-arrays pattern grown on Si substrate, b) Single rectangular PSi micro-array dimensions, c) Magnified image for the interface between Si and PSi, and d) the morphology of PSi grown into the micropattern.

3.2 Optical behavior

PSi can be regarded as a mixture of Si nanocrystallites, amorphous Si and air (pores) ^[18, 19]. Accordingly, its optical properties greatly depend on its porosity and thickness ^[22-25]. As a consequence, these parameters can be adjusted to produce high optical absorption in

a broad wavelength range. However, the reduction of the overall reflectance is accompanied by a decrease of electrical conductivity associated to a higher porosity and a higher oxidation degree [26, 27]. As such, the combination of silicon and PSi on the active layer can be an ideal strategy to combine in the same device the optical tunability of PSi and the high electrical conductivity of highly-doped Si. For this reason, rectangular micro-arrays of PSi were etched on the surface of photolithographic flat Si, termed Si+PSi micro-arrays.

Figure 5.a shows the comparison between the optical reflectance in the 250 to 900 nm wavelength range of flat Si, PSi (10 mA/cm², 10 s)/Si and (Si+PSi micro-arrays)/Si. The fabrication of a PSi layer onto Si results in a remarkable reduction of the overall reflectance, as expected, while the Si+PSi micro-arrays results only in a partial decrease in reflectance. The subsequent growth of the PEDOT:PSS thin film onto the surface of the different active layers leads to a further reduction of the optical reflectance in the three cases, as depicted in Figure 5.b. This effect is attributed to the anti-reflective properties of PEDOT:PSS [15, 20, 28]. The average reflectance (R_{av}) in the 250 nm-900 nm wavelength range was found to be 22.38%, 14.83 and 9.73% when PEDOT:PSS is grown onto Si, PSi and Si+PSi micro-arrays, respectively. In particular, the average reflectance of the Si+PSi micro-arrays coated with PEDOT:PSS is 33% lower than that of the PEDOT:PSS/Si junction, and almost 50 % lower in the central visible region

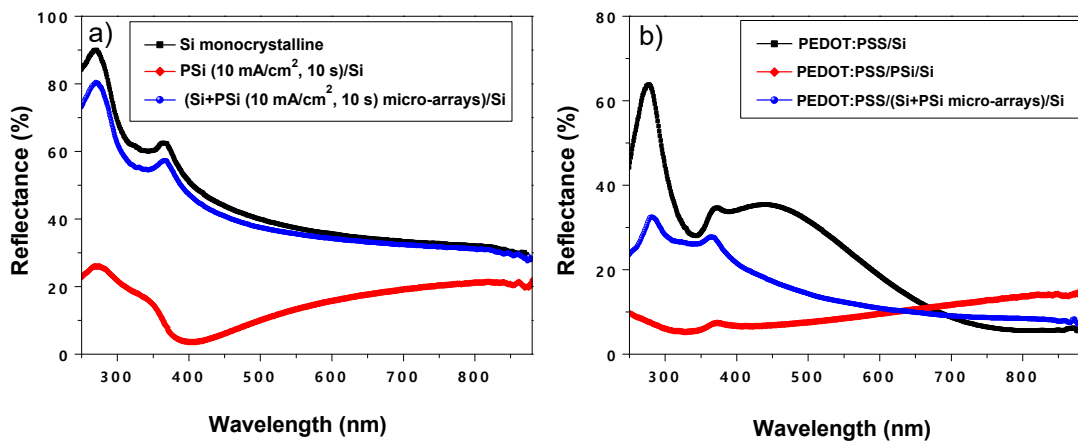


Figure 5: Typical optical reflectance in the 250 to 900 nm wavelength range. a) Reflectance for the active layers (Si, PSi/Si and (Si+PSi micro-arrays)/Si). b) Reflectance of PEDOT:PSS layer grown on Si, PSi/Si and (Si+PSi micro-arrays)/Si layers.

3.3 Electrical conduction and carrier transport characteristics

AC and DC electrical measurements were carried out aiming at studying the electrical conduction properties through the interfaces of the Si-based photodetectors. Figure 6.a portrays the I-V curves for the three devices in the -0.5 V to 0.5 V range from which a rectifying behavior is clearly observed in all cases. ~~In this regard, a thermionic emission carrier transport mechanism is assumed to be the dominant transport mechanism, as previously determined by other authors [29].~~ The rectifying behavior shown by the photodetectors under study confirms the contribution of PEDOT:PSS as a hole transport and electron blocking layer as discussed below in the energy band diagrams section. Accordingly, Si (or PSi/Si or (Si+PSi micro-arrays)/Si) is assumed to be the active layer responsible for the generation of the carriers. This assumption agrees with previous studies of devices based on PEDOT:PSS/Si junctions [12]. The Au/PEDOT:PSS/Si/Al devices show dark-current values higher than those of the modified Au/PEDOT:PSS/PSi/Si/Al devices, which can be attributed to the intrinsic low conductivity of PSi. However, the Au/PEDOT:PSS/(Si+PSi micro-arrays)/Si/Al devices show dark-current values close to those of the Au/PEDOT:PSS/Si/Al devices. This behavior is probably due to the contribution of the heavily-doped Si areas present in the structure of the active layer (Si+PSi micro-arrays), as shown in figure 4.a.

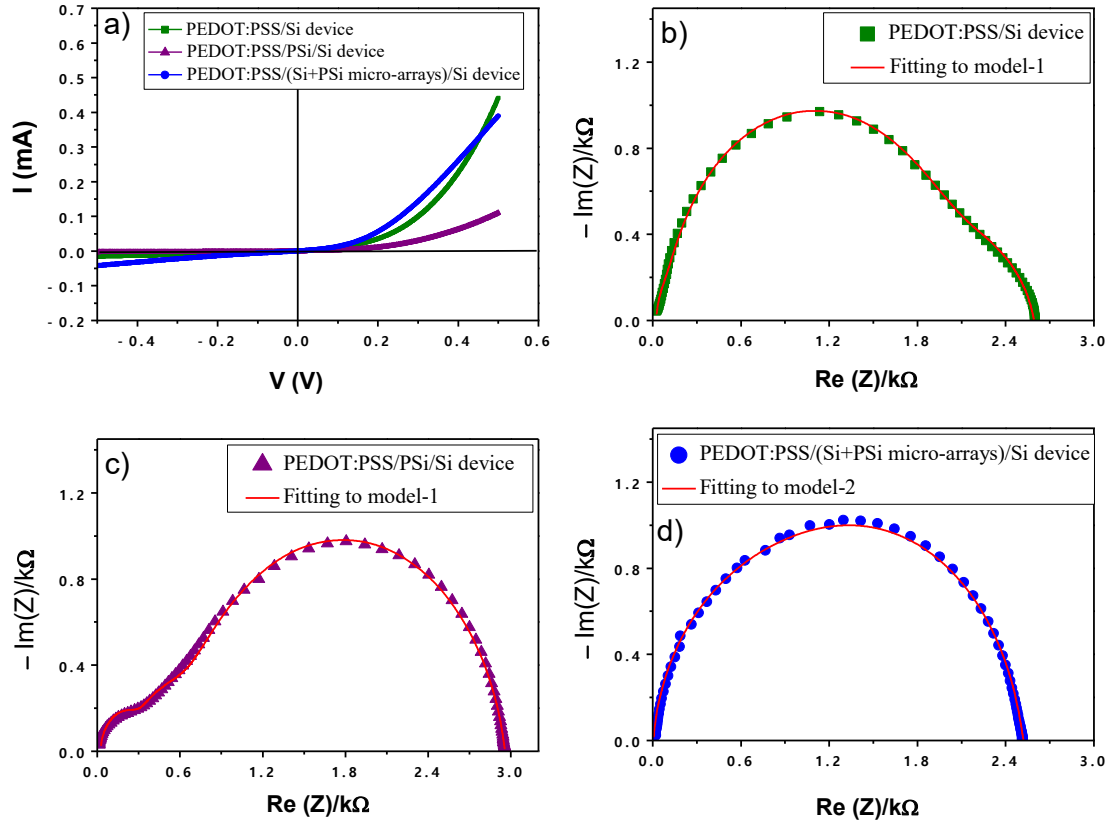


Figure 6: a) I–V curves for the three devices in the dark state. b) Nyquist plot for PEDOT:PSS/Si devices with the fitting to the equivalent circuit model-1. c) Nyquist plot for PEDOT:PSS/PSi/Si devices with the fitting to the equivalent circuit model-1. d) Nyquist plot for PEDOT:PSS/(Si+PSi micro-arrays)/Si devices with the fitting to the equivalent circuit model-2.

The electrical transport properties through the various interfaces of the photodetectors were studied by EIS. In this regard, Figures 6.b, 6.c and 6.d show the Nyquist plots for the Au/PEDOT:PSS/Si/Al, Au/PEDOT:PSS/PSi/Si/Al and Au/PEDOT:PSS/(Si+PSi micro-arrays)/Si/Al photodetectors, respectively. The measurements were carried out in the dark at 0 V bias. Figure 7 presents the most suitable equivalent circuit models which result from fitting the experimental data. The proposed models comprise one series resistance (R_s) and three additional circuits consisting of a resistor (R) in parallel with a capacitor (C). As indicated in Figure 7, each of these circuits has been associated to a specific interface in the device. The circuit associated to the active layer/PEDOT:PSS interface consists of a resistor in parallel with a constant phase element (Q). This element Q models an imperfect capacitor associated to inhomogeneity in composition or/and

thickness of the corresponding interface ^[30]. Thus, its characteristic capacitance, C , can be calculated with the following equation ^[31]:

$$C = Q_a \cdot R^{\frac{1-a}{a}} \quad (1)$$

where the factor a is an index that represents the degree of “perfection” of this element. This index can vary between 0 and 1, with 0 describing a perfect resistor, and 1 a perfect capacitor ^[30]. The Au/PEDOT:PSS/Si/Al and Au/PEDOT:PSS/PSi/Si/Al photodetectors were fitted to the same model, given in Figure 7.a. Figure 7.b shows the model corresponding to the Au/PEDOT:PSS/(Si+PSi micro-arrays)/Si/Al photodetectors. Table 1 summarizes the interfaces of the three Si-based photodetectors and the values of the electrical RC elements. Thereof, the R_s values for the three structures are rather small, which is an indication of the good overall properties of the metallic contacts.

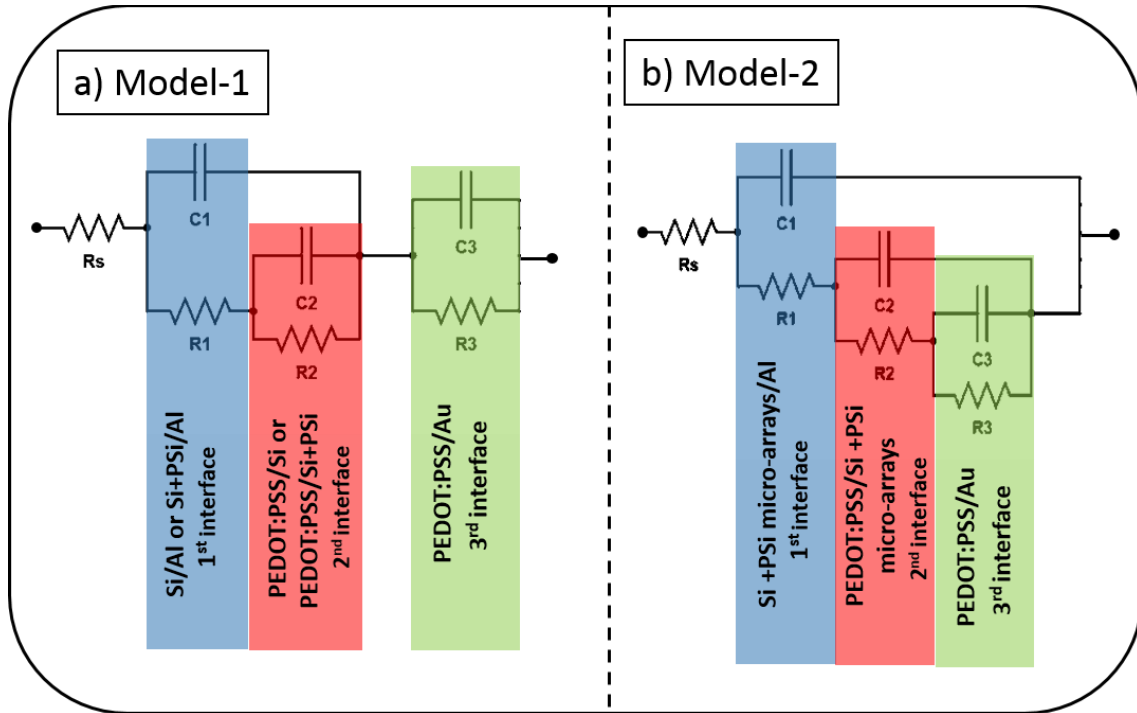


Figure 7: The equivalent circuit models with indication of the three interfaces. a) Model-1 used to fit the Au/PEDOT:PSS/Si/Al and Au/PEDOT:PSS/PSi/Si/Al photodetectors, b) Model-2 applied to fit the Au/PEDOT:PSS/(Si+PSi micro-arrays)/Si/Al photodetectors.

Table 1: Comparison between the electrical parameters obtained from the fitting of the Nyquist plots to the suitable equivalent circuit models.

Device structure	R _s (Ω)	R1 (k Ω)	C1 (nF)	R2 (k Ω)	Q1 $\mu\text{F.s}^{(a-1)}$	a1	C2 (nF)	R3 (Ω)	C3 (nF)
		1 st interface		2 nd interface			3 rd interface		
Au/PEDOT:PSS/Si/Al	26.14	1.91	23.49	0.55	4.16	0.82	52.7	98.80	36.47
Au/PEDOT:PSS/PSi/Si/Al	26.05	0.55	56.59	2.09	0.75	0.86	27.6	284	8.18
Au/PEDOT:PSS/(Si+PSi micro-arrays)/Si/Al	25.5	0.48	12	1.46	0.11	0.74	0.04	543.6	75.3

It is important to point out that the modifications in the structure of the active layers have a remarkable effect on the electrical parameters. For instance, the interface PEDOT:PSS/Si+PSi has a lower electrical conduction ($R_2 = 2.09 \text{ k}\Omega$) compared to that of the PEDOT:PSS/Si interface ($R_2 = 0.55 \text{ k}\Omega$). However, the PEDOT:PSS/Si+PSi micro-arrays interface shows better conduction properties, with $R_2 = 1.46 \text{ k}\Omega$. These results are in agreement with the results obtained from the analysis of the I-V curves in dark (Figure 6.a). For instance at 0.5 V, the Au/PEDOT:PSS/(Si+PSi micro-arrays)/Si/Al devices show comparable values of dark current with the basic Au/PEDOT:PSS/Si/Al devices. While, Au/PEDOT:PSS/PSi/Si/Al devices show lower value of dark current at the same bias.

3.4 Optoelectronic properties and photoresponse

3.4.1 Current- voltage characteristic under illumination

Figure 8 depicts the I-V curves for the Au/PEDOT:PSS/Si/Al photodetectors and the modified structures, i.e., Au/PEDOT:PSS/PSi/Si/Al and Au/PEDOT:PSS/(Si+PSi micro-arrays)/Si/Al, under different light irradiation intensities ranging from 100 mW/cm^2 to 1 mW/cm^2 . The experimental results clearly demonstrate the remarkable photovoltaic effect shown by the three devices. In all cases increased incident light power results in a notable increase in both photo-current (I_{ph}) and open-circuit voltage (V_{oc}). This behavior is attributed to the generation of electron-hole pairs as a result of the absorption of photons [32]. The specific mechanism of photo-carrier generation is discussed in the next section (energy band diagrams). I_{ph} for the Au/PEDOT:PSS/PSi/Si/Al devices is in general larger than that of the Au/PEDOT:PSS/Si/Al devices. However, under low levels of light irradiation (15 mW or lower), both I_{ph} and V_{oc} are slightly smaller. This behavior is associated to the reduction in the electrical conductivity by the PSi layer, as given in

Figure 6. At low irradiation, the photoresponse decreases and the carrier separation in the active layer is reduced. Complementary, the I-V curve for the Au/PEDOT:PSS/PSi/Si/Al device shows lower V_{oc} values compared to the base structure (Au/PEDOT:PSS/Si/Al).

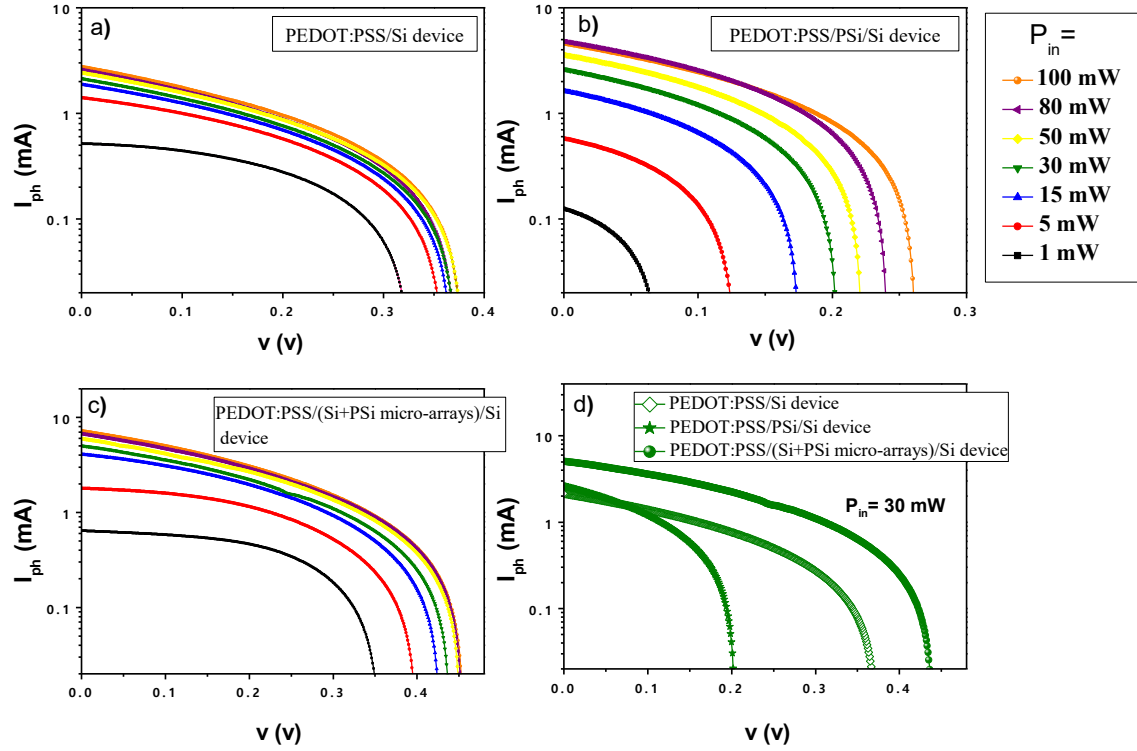


Figure 8: I-V curves of the photodetectors under different P_{in} and at 0 V bias. d) Comparison between the I-V curves for the three photodetectors at monocular P_{in} of 30 mW.

The reduction in the optical reflectance of the active layer of the photodetectors is not usually enough to enhance the overall photovoltaic performance over a wide range of light irradiation levels [33]. As such, Si+PSi micro-arrays were added to the basic structure, leading to devices with the structure Au/PEDOT:PSS/(Si+PSi micro-arrays)/Si/Al. These modified devices combine a reduction of the reflectance of the active layer associated to the presence of PSi micro-arrays (Figure 4.b) and limited electrical conduction losses (Figure 6). As a consequence of the structural modifications in the active layer surface, an outstanding performance for the Au/PEDOT:PSS/(Si+PSi micro-arrays)/Si/Al devices compared to the other devices fabricated is observed, as portrayed in Figure 8.c. Besides, Figure 8.d shows a comparison of the performance of the three devices at 30 mW incident power. A remarkable increment for the I_{ph} and the V_{oc} is observed for the devices with the Au/PEDOT:PSS/(Si+PSi micro-arrays)/Si/Al structure.

3.4.2 Energy band diagrams

The specific optoelectronic operation mechanisms of the photodetectors can be further analyzed from the energy band diagrams. Figure 9.a illustrates the energy band diagram that we propose for the Au/PEDOT:PSS/Si/Al photodetectors. The lowest unoccupied molecular orbital (LUMO) and the highest occupied molecular orbital (HOMO) of PEDOT:PSS are estimated to be 3.5 and 5.0 eV, respectively ^[16]. As for silicon, the conduction band minimum (CB) and valence band maximum (VB) levels are reported to be 4.05 and 5.15 eV, respectively ^[34]. The PEDOT:PSS and Si junction results in a small valence band offset ($\Delta E_v = 0.15 \text{ eV}$) and a higher conduction band offset ($\Delta E_c = 0.55 \text{ eV}$). Upon illumination with light of energy greater than the bandgap energy of Si, absorption of photons would result in the generation of electron-hole pairs that will move in opposite directions. While PEDOT:PSS is a p-type semiconductor with high electrical conduction, it is not considered to be responsible for the generation of photocarriers when exposed to light ^[11], given that charge carriers are strongly bound. For this reason, PEDOT:PSS is considered to act as a hole transport and electron blocking layer due to its hole selective conductivity ^[35, 36]. Accordingly, photocarriers will be mainly generated in Si ^[12]. Electrons will drift to the Si side (Al contact), whereas holes will drift to the PEDOT:PSS side (Au contact), both charge carriers contributing to the total photocurrent.

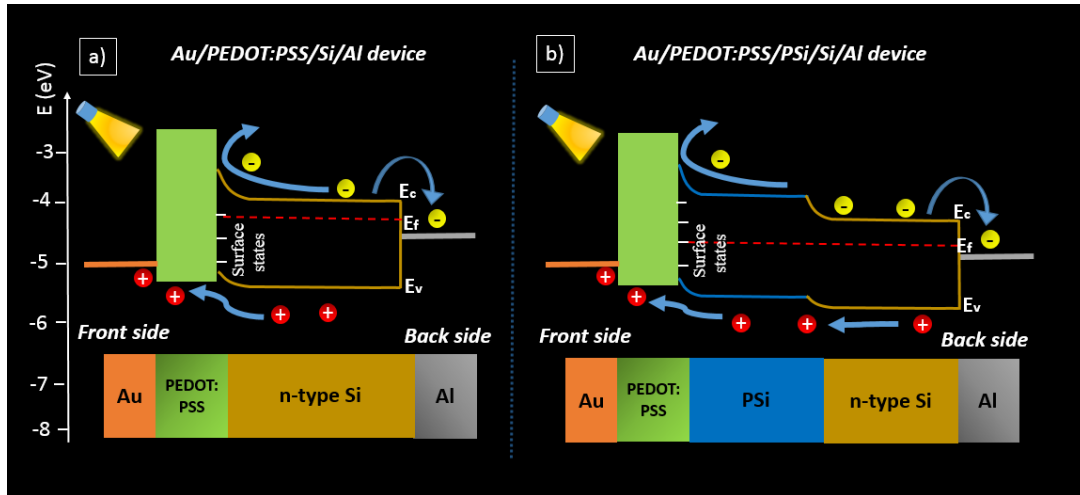


Figure 9: The proposed energy band diagram. a) Correspond to Au/PEDOT:PSS/Si/Al devices. b) Correspond to Au/PEDOT:PSS/PSi/Si/Al devices.

Figure 9.b shows the proposed energy band diagram for the Au/PEDOT:PSS/PSi/Si/Al photodetectors. The Fermi level for the PSi layer is located close to the middle of the energy gap. This assumption is a consequence of the formation of the nanopores at dopant sites of Si ^[17], which leads to a widening of the energy bandgap of PSi with respect to that of Si (1.12 eV). Under illumination, the generated photocurrent follows the same mechanism as in the Au/PEDOT:PSS/Si/Al devices. Besides, the increase in the number of generated carriers at high irradiation intensities is attributed to the optical absorption enhancement provided by the PSi layer. However, the decrease in the V_{oc} and I_{ph} at low intensities is related to the low electrical conductivity of the PSi layer, leading to lower mobility and transport ^[37]. Also, the surface states between PSi and PEDOT:PSS layer increase.

As for the Au/PEDOT:PSS/(Si+PSi micro-arrays)/Si/Al photodetectors, their electrical behavior can be considered as a combination in parallel of the electrical conduction mechanisms previously discussed for the Au/PEDOT:PSS/Si/Al and Au/PEDOT:PSS/PSi/Si/Al devices. As a consequence of the combination of the two conduction mechanisms, I_{ph} and V_{oc} were greatly enhanced over a wide range of light irradiation levels.

3.4.3 Time-dependent photoresponse analysis

Repeatability and reproducibility of the electrical response of photodetectors to pulsed light can be determined from current-time (I-t) curves. Figures 10.a, 10.b and 10.c reveal that the self-powered photodetectors show a rapid response when light is switched on, and the photocurrent drops back to zero when it is switched off. Furthermore, it can be observed that the photodetectors show an excellent repeatability and reproducibility to pulsed light over a wide range of irradiation powers since the output signal remains the same over a large number of cycles. Figure 10 shows how the photocurrent increases for the three devices when the incident power increases. More specifically, the Au/PEDOT:PSS/(Si+PSi micro-arrays)/Si/Al devices show the highest photocurrent values. As discussed above, this result is attributed to the reduction of reflectance of the active layer due to the presence of PSi and the limited electrical conduction losses. The large difference between the dark current and the photocurrent for the three devices indicates that the photodetectors have excellent sensitivity to incident light in a wide range

of light intensities (from 100 μW to 100 mW). For instance, at 0 V bias and under 30 mW incident power, the current of the Au/PEDOT:PSS/Si/Al, Au/PEDOT:PSS/PSi/Al and Au/PEDOT:PSS/PSi micro-arrays/Al devices increased dramatically from 9.3×10^{-4} , 2.67×10^{-4} and 8.18×10^{-4} mA in the dark state to 2.13, 2.5 and 5.17 mA, respectively. Accordingly, the current ratio ($I_{\text{on}}/I_{\text{off}}$) is around 10^4 .

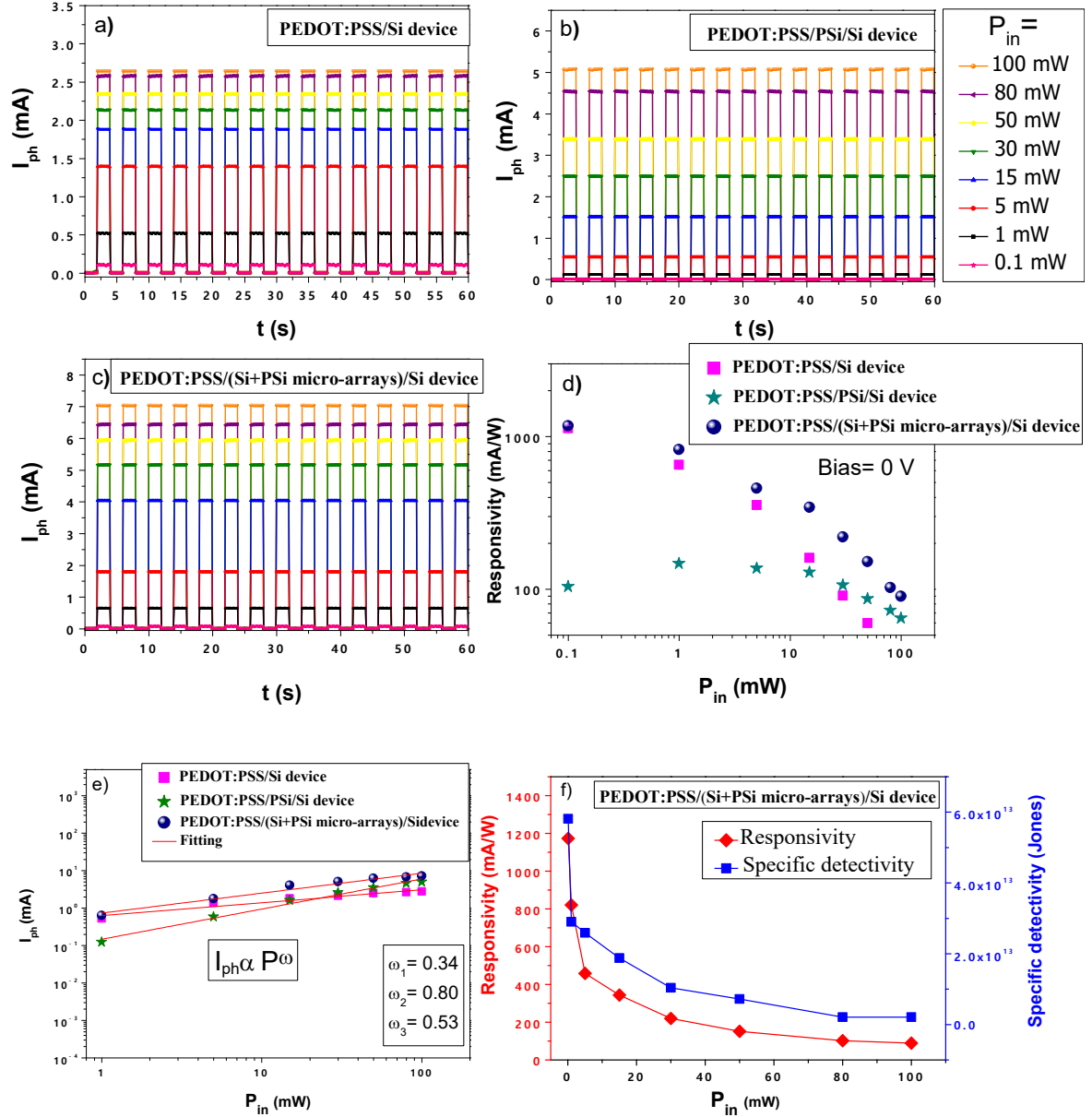


Figure 10: Time-dependent photo-response (I - t) curves measured under irradiation with different P_{in} . a) Corresponds to Au/PEDOT:PSS/Si/Al photodetectors, b) Corresponds to Au/PEDOT:PSS/PSi/Si/Al photodetectors and c) Corresponds to Au/PEDOT:PSS/(Si+PSi micro-arrays)/Si/Al photodetectors. d) The dependence of responsivity of the three photodetectors with P_{in} at 0 V bias. e) Logarithmic plot of the I_{ph} versus P_{in} at 0 V bias. f) The dependence of

responsivity and specific detectivity of the Au/PEDOT:PSS/(Si+PSi micro-arrays)/Si/Al photodetectors with P_{in} .

Figure 10.d shows the dependence of the responsivity on the power of the incident light. This value can be calculated from the following equation ^[14]:

$$\text{Responsivity} = \frac{(I_{ph} - I_d)}{P_{in} \cdot S} \quad (2)$$

where I_{ph} is the photocurrent, I_d is the dark current, P_{in} is the incident power density and S is the active area of the photodetectors (0.785 cm² in our case). According to our results shown in Figure 10.d, the Au/PEDOT:PSS/Si/Al devices show high values of responsivity at low irradiation levels, while the Au/PEDOT:PSS/PSi/Si/Al devices show higher values under high levels of irradiation. As for Au/PEDOT:PSS/(Si+PSi micro-arrays)/Si/Al photodetectors, the experimental results confirm a remarkable performance in a wide range of incident powers. For instance, at a low incident power of 100 μ W, the responsivity values are 1130.14, 103.60 and 1172.87 mA/W for the devices Au/PEDOT:PSS/Si/Al, Au/PEDOT:PSS/PSi/Si/Al and Au/PEDOT:PSS/(Si+PSi micro-arrays)/Si/Al, respectively. While at high intensity of 100 mW, the responsivity values are 33.61, 64.51 and 89.50 mA/W, respectively (Figure 10.d). From this perspective, the integration between PSi and Si micro-nanostructures results in a remarkable improvement in the optoelectronic response of the photovoltaic photodetectors.

As a consequence of the sensitivity of the photodetectors to the optical signals, additional photoresponse analysis was carried out. Figure 10.e shows the dependence of I_{ph} with P_{in} , which can be fitted to the following power law ^[14]:

$$I_{ph} = A \cdot P_{in}^\omega \quad (3)$$

where I_{ph} and P_{in} are the photocurrent and the incident light power, respectively, A is a proportional constant and ω is a factor related to generation and recombination processes in the active layer of the photodetectors ^[38]. A value of 1 indicates ideal generation of electron-hole pairs. By fitting the data in figure 10.e to equation 3, the values of ω were found to be 0.34, 0.80 and 0.53 for Au/PEDOT:PSS/Si/Al, Au/PEDOT:PSS/PSi/Si/Al and Au/PEDOT:PSS/(Si+PSi micro-arrays)/Si/Al, respectively. Lower values of ω are

attributed to carrier recombination due to the presence of defects in the active layer. The highest value corresponds to the Au/PEDOT:PSS/PSi/Si/Al devices, which might be attributed to the dramatic degradation in I_{ph} with the reduction of P_{in} . This behavior leads to a relation between I_{ph} and P_{in} close to unity.

The ability of the photodetectors to detect small light signals is a parameter defined by the specific detectivity (D^*). D^* can be calculated from the following equation ^[14]:

$$D^* = \text{Responsivity} \cdot \sqrt{\frac{A}{(2 \cdot q \cdot I_d)}} \quad (4)$$

where A is the total area of the device (0.785 cm^2 in this work), q is the elementary charge ($1.602 \times 10^{-19} \text{ C}$) and I_d is the dark current. Figure 10.f reveals the remarkable efficiency (Responsivity and Detectivity) of the complementary Au/PEDOT:PSS/(Si+PSi micro-arrays)/Si/Al devices in a wide range of incident light powers.

It is important to determine the response speed of the photodetectors since it reflects the ability of the device to respond to fast switching optical signals. Figures 11.a, 11.b and 11.c show the on/off response speed for the Au/PEDOT:PSS/Si/Al, Au/PEDOT:PSS/PSi/Si/Al and Au/PEDOT:PSS/(Si+PSi micro-arrays)/Si/Al photodetectors, respectively. The analysis was carried out by switching $400 \text{ }\mu\text{W}$ white light every 20 ms at 50 Hz and 0 V bias. The table in figure 11.d presents a comparison of the rise (t_r) and fall times (t_f) for the three detectors. It can be seen that the three devices have the ability to respond to fast light switching with excellent reproducibility and stability. It is also observed that the Au/PEDOT:PSS/Si/Al photodetectors give the fastest response (shorter than $217 \text{ }\mu\text{s}$ / $387 \text{ }\mu\text{s}$ respectively). This behavior is probably due to the small amount of defects in the Si surface, i.e., the active layer, compared with an active layer composed of PSi. Since PSi causes an increase in the number of surface states as demonstrated in the energy band diagrams (Figure 9). Thus, the surface states increase the rate of carrier recombination, which hinders the response speed of the photodetectors.

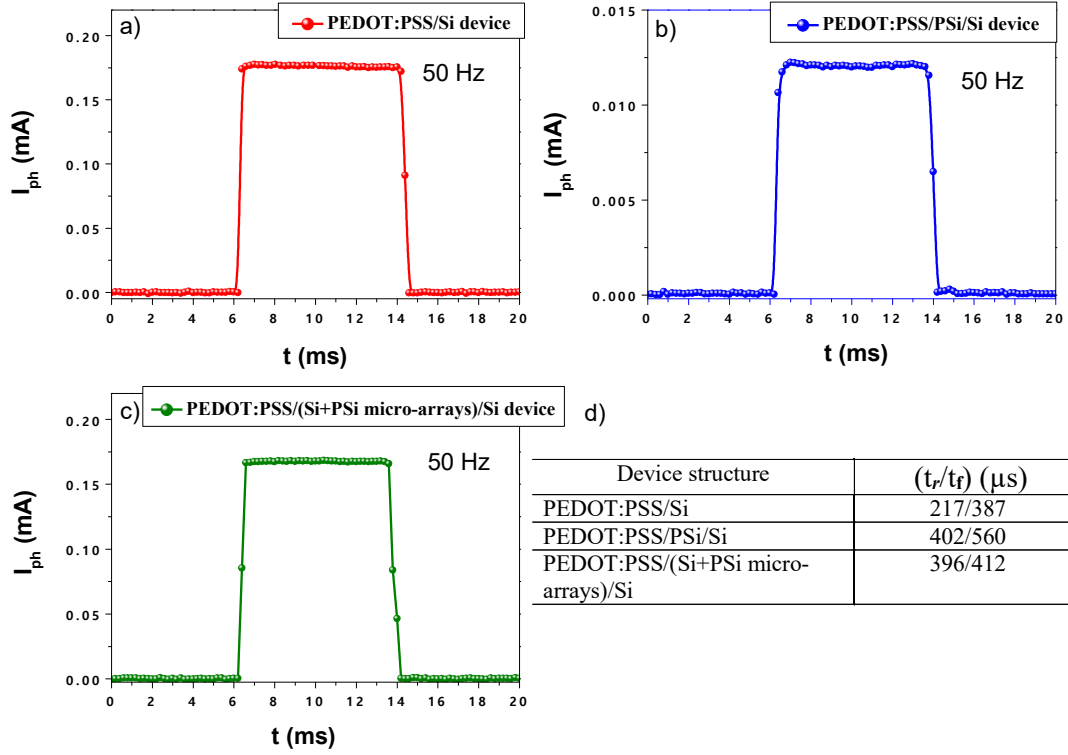


Figure 11: The response speed of the photodetectors under fast switching with (400 μ W) at 50 Hz and 0 V bias. a) Response speed for Au/PEDOT:PSS/Si/Al photodetectors, b) Response speed for Au/PEDOT:PSS/PSi/Si/Al photodetectors, and c) Response speed for Au/PEDOT:PSS/(Si+PSi micro-arrays)/Si/Al photodetectors. d) Table gives the obtained values of rise time and fall time of the three photodetectors.

Table 2: Comparison of the device performances of some reported photodetectors based on Si nanostructures or/and PEDOT:PSS thin films.

Device structure	Bias (V)	Responsivity (mA/W)	D* (Jones)	Rise/fall time (μ s)	Ref.
CuO/Si nanowire arrays	0	0.389 @ 405 nm	3.00×10^9	60/80 @ 1000 Hz	[39]
ZnO nanostructure array/PSi	3	1980 @ 325 nm	...	86000/83000	[40]
CH ₃ NH ₃ PbI ₃ thin films/PSi pillar array	0	8.13 @ 780 nm	0.974×10^{13}	253.3/230.4 @ 800 Hz	[14]
PEDOT:PSS/SnO ₂ microwires	0	18.2 @ 450 nm	[10]
PEDOT:PSS/single Se microtube	0	5.5 @ 610 nm	1.76×10^{10}	1000/9780	[41]
ZnO/PEDOT:PSS	1	13 @ 380 nm	...	270000/280000 @ 0.5 Hz	[42]

(PEDOT:PSS)/Ga ₂ O ₃	0	37.4 @ 254 nm	9.2×10^{12}	3.3/71.2	[11]
Graphene/ PEDOT:PSS	0	160 @ 500 nm	1.33×10^{12}	...	[43]
PEDOT:PSS/Si nanowire arrays (820 nm length)	0	37.8 @ 920 nm	4.1×10^{11}	3.17/55.4 @ 1000 Hz	[12]
PEDOT:PSS/(Si+PSi micro-arrays)	0	1172.8 @ white light	5.81×10^{13}	396/412 @ 50 Hz	Present work

Table 2 shows a comparison between the obtained characteristic parameters for the modified devices with previously reported values. The comparison is for photodetectors based on the same materials (Si nanostructures or/and PEDOT:PSS thin films). The results show how the combination of silicon and PSi on the same surface can be an ideal strategy to improve the photovoltaic response of self-powered photodetectors in a wide range of incident powers.

3.4.4 Spectral responsivity

Figure 12.a shows the spectral responsivity of the photodetectors in the 300 to 1200 nm wavelength range and at 0 V bias. The experimental results show that the photoresponse spectrum for the Au/PEDOT:PSS/Si/Al devices shows a wideband response in the visible and near-infrared regions, although responsivity diminishes for wavelengths over 1000 nm. This behavior is attributed to the use of radiation with photon energy less than the energy bandgap of the active layer, i.e., Si (~around 1110nm) [34], resulting in reduced absorption. The spectral responsivity of the Au/PEDOT:PSS/PSi/Si/Al photodetectors is higher in the near-infrared region than in the visible, which is attributed to the lower transparency and higher dispersion of PSi in the visible region. However, the overall responsivity is noticeably lower than in the previous device, which is attributed to two reasons. (1) The reduction in the electrical conductivity associated to the presence of PSi layer. (2) The increase in the surface-to-volume ratio of the PSi layer, which results in increased electron-hole recombination rates. Figure 12.a shows that the maximum responsivity for the Au/PEDOT:PSS/PSi/Si/Al photodetectors is 265.56 mA/W at 1007 nm. This wavelength corresponds to a photon energy of 1.24 eV, which is assumed to be the energy bandgap of the PSi layer. The increase in the energy bandgap values of PSi

compared to the bulk Si wafer (1.12 eV) is considered to be a manifestation of quantum confinement effects [18, 19]. A similar behavior was previously found for PSi-based photodetectors with a peak responsivity of 77 mA/W at 780 nm, where the diameter of the pores was around 12 nm [44].

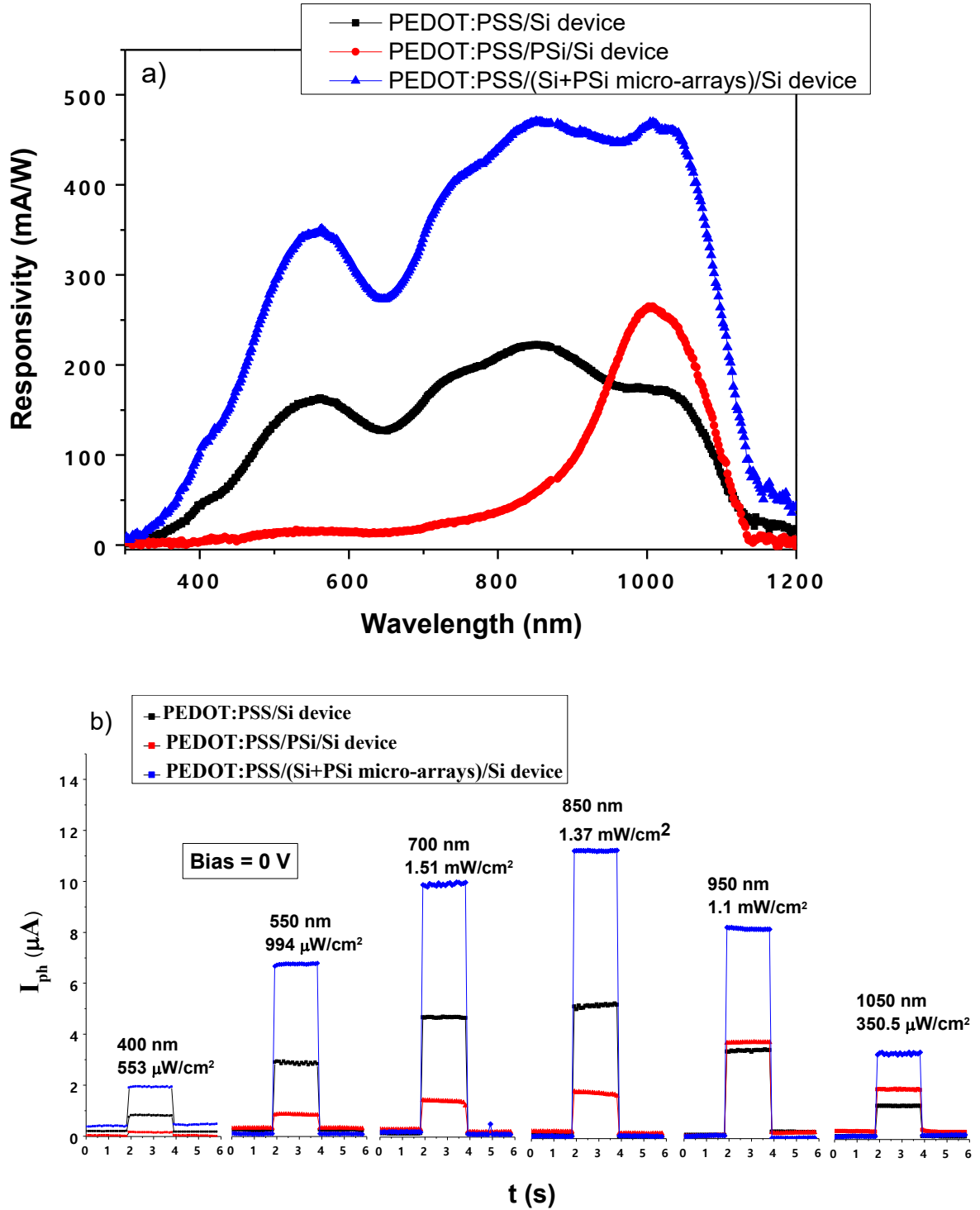


Figure 12: a) The spectral responsivity of the three photodetectors in the wavelength 300 to 1200 nm range at 0 V bias. b) I–t curves of the three devices under irradiation with different intensities of monochromatic light at 0 V bias.

The Au/PEDOT:PSS/(Si+PSi micro-arrays)/Si/Al photodetectors show an improved performance over a broad range of the optical spectrum. The mechanisms behind this behavior is associated to two main reasons. First, the optical enhancement in the visible and near-infrared regions by the presence of a thin layer of PSi micro-arrays. Second, the electrical conduction is improved by the presence in the active layer of heavily-doped Si regions. In this case two parallel conduction mechanisms contribute to the generation of photocarriers. The first generation path is through the PEDOT:PSS/PSi/Si interfaces and the second occurs through the PEDOT:PSS/Si interface. As such, the output photocurrent is enhanced over all the wavelength range. Besides, the remarkable enhancement observed in Figures 8 and 10 confirms the extraordinary sensitivity of the Au/PEDOT:PSS/(Si+PSi micro-arrays)/Si/Al photodetectors to white light in a wide range of incident light powers.

Figure 12.b demonstrates an effective photoresponse of the self-powered photodetectors to monochromatic light of different wavelengths. The modified Au/PEDOT:PSS/PSi/Si/Al photodetectors outperform the Au/PEDOT:PSS/Si/Al devices in the infrared region and vice versa in the UV-visible regions. Furthermore, the Au/PEDOT:PSS/(Si+PSi micro-arrays)/Si/Al photodetectors always show the best photoresponse from the near-UV to the IR regions.

Conclusions

The main aim of the current work was to develop highly-stable, reliable, high-efficiency, and fast response broadband self-powered photodetectors. We have investigated three different device configurations of hybrid organic-inorganic photodetectors, namely Au/PEDOT:PSS/Si/Al, Au/PEDOT:PSS/PSi/Si/Al, and Au/PEDOT:PSS/(Si+PSi micro-array)/Si/Al. The structural modifications introduced on the surface of Si have a notable effect on the reflectance, electrical conduction, and photoresponse of the photodetectors.

The specific mechanism of photo-carrier generation was studied, and energy band diagrams for the devices were proposed.

It is worth pointing out that the average reflectance in the 250 nm-900 nm wavelength range of the Si+PSi micro-arrays is higher than that of the PSi layer. Besides, the etching of a PSi layer leads to a reduction in the electrical conduction. Meanwhile, the integrated structure of Si+PSi micro-arrays provides dark current values close to those for the devices based on flat Si.

The experimental results reveal that the three configurations exhibit excellent stability and reproducibility over a wide range of incident light powers. However, the Au/PEDOT:PSS/Si/Al devices show high values of responsivity at low irradiation levels, while the Au/PEDOT:PSS/PSi/Si/Al devices show high values under high levels of irradiation. As for Au/PEDOT:PSS/(Si+PSi micro-array)/Si/Al photodetectors, an outstanding performance over a wide range of incident powers was demonstrated.

As for the spectral responsivity, the Au/PEDOT:PSS/Si/Al devices show a wideband response in the visible and near-infrared regions. The Au/PEDOT:PSS/PSi/Si/Al devices show a narrowband response in the near-infrared region which is attributed to the morphology of the PSi layers. The Au/PEDOT:PSS/(Si+PSi micro-array)/Si/Al photodetectors show a remarkable performance over a broad wavelength range of the optical spectrum. As such, the combination of Si and PSi on the same surface can be an ideal strategy to obtain in the same device the tunability of the optical behavior of PSi and the rather large electrical conduction of highly-doped Si, leading to highly-efficient photonic devices.

Author contributions: Conceptualization (R. Ramadan and R.J. Martín-Palma), Formal Analysis (R. Ramadan, V. Torres-Costa and R.J. Martín-Palma), Funding acquisition (R. Ramadan, V. Torres-Costa and R.J. Martín-Palma), Investigation (R. Ramadan, V. Torres-Costa and R.J. Martín-Palma), Methodology (R. Ramadan), Project administration (R.J. Martín-Palma), Supervision (R.J. Martín-Palma), Validation (R. Ramadan, V. Torres-Costa and R.J. Martín-Palma), Visualization (R. Ramadan), Writing – original draft (R. Ramadan), Writing – review & editing (R. Ramadan, V. Torres-Costa and R.J. Martín-Palma).

Funding: This research was partially funded by Universidad Autónoma de Madrid, FPI-UAM grant and by the Egyptian Ministry of Higher Education, Missions Section under Egyptian Joint Supervision Grant. This work was part of ATTRACT that has received funding from the European Union's Horizon 2020 Research and Innovation Programme.

Acknowledgments: The authors are thankful to Mr. Luis García Pelayo and Dr. Valentin Constantin Nistor for their technical support.

Conflicts of Interest: The authors declare no conflict of interest.

References

- [1] H. S. Nalwa, *Photodetectors and fiber optics*, Elsevier, 2012.
- [2] W. Tian, H. Zhou, L. Li, *Small*, **2017**, 13, 1702107.
- [3] M. Ahmadi, T. Wu, B. Hu, *Advanced Materials*, **2017**, 29, 1605242.
- [4] Y. Zhao, C. Li, L. Shen, *InfoMat*, **2019**, 1, 164.
- [5] J. Zhou, J. Huang, *Advanced Science*, **2018**, 5, 1700256.
- [6] X. Wang, W. Song, B. Liu, G. Chen, D. Chen, C. Zhou, G. Shen, *Advanced Functional Materials*, **2013**, 23, 1202.
- [7] L. Li, F. Zhang, W. Wang, Q. An, J. Wang, Q. Sun, M. Zhang, *ACS applied materials & interfaces*, **2015**, 7, 5890.
- [8] M. Kielar, O. Dhez, G. Pecastaings, A. Curutchet, L. Hirsch, *Scientific reports*, **2016**, 6, 39201.
- [9] B. Friedel, P. E. Keivanidis, T. J. Brenner, A. Abrusci, C. R. McNeill, R. H. Friend, N. C. Greenham, *Macromolecules*, **2009**, 42, 6741.
- [10] S. Li, S. Wang, K. Liu, N. Zhang, Z. Zhong, H. Long, G. Fang, *Applied Physics A*, **2015**, 119, 1561.
- [11] S. Li, Z. Yan, Z. Liu, J. Chen, Y. Zhi, D. Guo, P. Li, Z. Wu, W. Tang, *Journal of Materials Chemistry C*, **2020**, 8, 1292.
- [12] Z. Liang, P. Zeng, P. Liu, C. Zhao, W. Xie, W. Mai, *ACS applied materials & interfaces*, **2016**, 8, 19158.
- [13] J. A. Nelson, *The physics of solar cells*, World Scientific Publishing Company, 2003.
- [14] Y. Cheng, Z. Shi, S. Yin, Y. Li, S. Li, W. Liang, D. Wu, Y. Tian, X. Li, *Solar Energy Materials and Solar Cells*, **2020**, 204, 110230.
- [15] D. Samajdar, *Solar Energy*, **2019**, 190, 278.
- [16] W. Chen, P. Gao, L. Zhou, L.-H. Shi, D.-W. Wang, R. Hao, J. Ye, W.-Y. Yin, E. Li, *IEEE Journal of Photovoltaics*, **2018**, 8, 757.
- [17] D. H. Shin, J. H. Kim, J. H. Kim, C. W. Jang, S. W. Seo, H. S. Lee, S. Kim, S.-H. Choi, *Journal of Alloys and Compounds*, **2017**, 715, 291.
- [18] R. Martín-Palma, L. Pascual, P. Herrero, J. Martínez-Duart, *Applied physics letters*, **2002**, 81, 25.
- [19] R. Martín-Palma, L. Pascual, P. Herrero, J. Martínez-Duart, *Applied Physics Letters*, **2005**, 87, 211906.
- [20] J. P. Thomas, K. T. Leung, *Advanced Functional Materials*, **2014**, 24, 4978.

- [21] R. J. Martín-Palma, P. D. McAtee, R. Ramadan, A. Lakhtakia, *Scientific reports*, **2019**, 9, 7291.
- [22] R. Ramadan, M. Manso-Silván, R. J. Martín-Palma, *Journal of Materials Science*, **2020**, 55, 5458.
- [23] R. J. Martín-Palma, P. D. McAtee, R. Ramadan, A. Lakhtakia, *Scientific reports*, **2019**, 9, 1.
- [24] I. Sagnes, A. Halimaoui, G. Vincent, P. Badoz, *Applied physics letters*, **1993**, 62, 1155.
- [25] V. Torres-Costa, R. Martín-Palma, *Journal of materials science*, **2010**, 45, 2823.
- [26] R. C. Anderson, R. S. Muller, C. W. Tobias, *Journal of the Electrochemical Society*, **1991**, 138, 3406.
- [27] R. Ramadan, R. J. Martín-Palma, *Energies*, **2020**, 13, 2165.
- [28] J. P. Thomas, K. T. Leung, *Journal of Materials Chemistry A*, **2016**, 4, 17537.
- [29] J. Henning, K. Schoen, M. Melloch, J. Woodall, J. Cooper, *Journal of electronic materials*, **1998**, 27, 296.
- [30] M. E. Orazem, B. Tribollet, *Electrochemical impedance spectroscopy*, John Wiley & Sons, 2017.
- [31] D. Ribeiro, C. Souza, J. Abrantes, *Revista IBRACON de Estruturas e Materiais*, **2015**, 8, 529.
- [32] F. Scholze, H. Rabus, G. Ulm, *Journal of Applied Physics*, **1998**, 84, 2926.
- [33] W. Ouyang, F. Teng, J. H. He, X. Fang, *Advanced Functional Materials*, **2019**, 29, 1807672.
- [34] J. Nelson, *The physics of solar cells*, World Scientific Publishing Company, 2003.
- [35] M. Yi, S. Hong, J.-R. Kim, H. Kang, J. Lee, K. Yu, S. Kee, W. Lee, K. Lee, *Solar Energy Materials and Solar Cells*, **2016**, 153, 117.
- [36] S. Rafique, S. M. Abdullah, M. M. Shahid, M. O. Ansari, K. Sulaiman, *Scientific reports*, **2017**, 7, 39555.
- [37] H. Zhang, C. Wang, W. Peng, C. Yang, X. Zhong, *Nano Energy*, **2016**, 23, 60.
- [38] Y. Li, Z. Shi, L. Lei, Z. Ma, F. Zhang, S. Li, D. Wu, T. Xu, X. Li, C. Shan, *ACS Photonics*, **2018**, 5, 2524.
- [39] Q. Hong, Y. Cao, J. Xu, H. Lu, J. He, J.-L. Sun, *ACS applied materials & interfaces*, **2014**, 6, 20887.
- [40] R. Dalvand, S. Mahmud, R. Shabannia, *Journal of Materials Science: Materials in Electronics*, **2018**, 29, 4999.
- [41] P. Yu, K. Hu, H. Chen, L. Zheng, X. Fang, *Advanced Functional Materials*, **2017**, 27, 1703166.
- [42] N. Hernandez-Como, G. Rivas-Montes, F. Hernandez-Cuevas, I. Mejia, J. Molinar-Solis, M. Aleman, *Materials Science in Semiconductor Processing*, **2015**, 37, 14.
- [43] Z. Liu, K. Parvez, R. Li, R. Dong, X. Feng, K. Müllen, *Advanced Materials*, **2015**, 27, 669.
- [44] K.-H. Wu, C.-W. Li, J.-H. Liu, *Microelectronic Engineering*, **2015**, 148, 70.